Journal of Geophysical Research: Space Physics

RESEARCH ARTICLE
10.1002/2017JA024291

Spatial and Temporal Ionospheric Monitoring Using Broadband Sferic Measurements

J. C. McCormick[1], M. B. Cohen[1], N. C. Gross[1], and R. K. Said[2]

[1]Department of Electrical and Computer Engineering, Georgia Institute of Technology, Atlanta, GA, USA, [2]Vaisala Inc., Louisville, CO, USA

Key Points:
- With the described algorithm, we can adjust for the natural variability of lightning sources and for errors in geolocation
- By comparison to a propagation model, we can produce globally applicable ionospheric inferences with no feature constraints
- We describe a new approach for removal of narrowband navy transmitters from the data record which outperforms notch filtering

Correspondence to:
J. C. McCormick,
jcmccorm@gatech.edu

Citation:
McCormick, J. C., Cohen, M. B., Gross, N. C., & Said, R. K. (2018). Spatial and temporal ionospheric monitoring using broadband sferic measurements. *Journal of Geophysical Research: Space Physics*, *123*, 3111–3130. https://doi.org/10.1002/2017JA024291

Received 24 APR 2017
Accepted 9 MAR 2018
Accepted article online 30 MAR 2018
Published online 21 APR 2018

Abstract The *D* region of the ionosphere (60–90 km altitude) is highly variable on timescales from fractions of a second to many hours, and on spatial scales up to many hundreds of kilometers. Very low frequency (VLF) and low-frequency (LF) (3–30 kHz and 30–300 kHz) radio waves are guided to global distances by reflections from the ground and the *D* region. Therefore, information about its current state is encoded in received VLF/LF signals. VLF transmitters have been used in the past for *D* region studies, with ionospheric disturbances manifesting as perturbations in amplitude and/or phase. The return stroke of lightning is an impulsive VLF radiator, but unlike VLF transmitters, lightning events are distributed broadly in space allowing for much greater spatial coverage of the *D* region compared to VLF transmitter-based remote sensing in addition to the broadband spectral advantage over the narrowband transmitters. The challenge is that individual lightning-generated waveforms, or "sferics," vary due to the lightning current parameters and uncertainty in the time/location information, in addition to *D* region ionospheric variability. These factors make it difficult to utilize the VLF/LF emissions from lightning in a straightforward manner. We describe a technique to recover the time domain and amplitude/phase spectra for both Bϕ and B*r* with high fidelity and consider the utility of our technique with ambient and varied ionospheric conditions. We demonstrate a technique to simulate sferics and infer a parameterized ionosphere with the Wait and Spies parameters (h' and β) offering all of the tools needed for a global measurement.

1. Introduction

The *D* region of the ionosphere (60–90 km) is a relatively inaccessible but important region for subionospheric radio propagation. It consists of cold collisional plasma that efficiently reflects waves at lower frequencies with some amount of loss and dispersion while causing significant losses to high-frequency (HF, 3–30 MHz) propagation which slowly refracts through the upper ionosphere after passing through the *D* region. The *D* region electron density varies due to solar effects over diurnal, seasonal, and solar cycle periods. It also varies on smaller spatial and time scales due to unpredictable transient perturbations such as solar flares as discussed in Mitra (1964), lasting minutes to hours and affecting the entire dayside ionosphere; lightning-induced electron precipitation described in Helliwell et al. (1973), lasting tens of seconds to minutes and hundreds of kilometers in extent usually observed in the nighttime *D* region ionosphere; electrodynamic heating from lightning (Inan et al., 1991), lasting up to tens of minutes and tens of kilometers in extent also typically observed in the nighttime *D* region ionosphere; or the winter anomaly *D* region as described by Sechrist et al. (1969) causing an enhancement of *D* region electron density for days or weeks. The *D* region also varies on a latitudinal basis, for example, the polar regions are dominated by particle precipitation and in strong events there is significant perturbation to the *D* region causing abnormal HF absorption known as polar cap absorption (Megill et al., 1971). Furthermore, the occurrence and extent of solar eclipses is well known, but the effect on *D* region densities and wave propagation is not yet fully understood (Clilverd et al., 2001). The unperturbed nighttime *D* region is ionized primarily by galactic cosmic rays, X-rays (<1 nm), and Lyman-α (121.6 nm) radiation emission from hydrogen. The daytime ambient ionosphere ionization is dominated by Lyman-α radiation (Kockarts, 2002). However, during an X-ray solar flare, the *D* region ionization is dominated by the photoionization of the atmospheric gases (Grubor et al., 2008).

The electron densities of the *E* and *F* regions of the ionosphere (100–500 km) can be measured more readily by radars or by HF propagation (Alfonsi et al., 2008) to produce reasonably accurate electron density profile estimates, many of which are included in the empirically constructed International Reference Ionosphere

(Bilitza et al., 2011). However, the *D* region is much more difficult to characterize as it is too high for balloons and too low for satellites, not sufficiently ionized for radars, and responds to different geophysical drivers than the *E* and *F* regions. The International Reference Ionosphere therefore is much less reliable for estimating *D* region parameters. Rocket-based measurements produce good ionospheric profile results (Friedrich & Torkar, 2001; Kintner et al., 1983; Sechrist, 1974), but they cannot realistically be applied on a continuous and global basis.

Terrestrial very low frequency (VLF, 3–30 kHz) and low-frequency (LF, 30–300 kHz) waves propagate to great distances (>2 Mm) (Higginson-Rollins & Cohen, 2017) guided by the Earth ground and the *D* region of the ionosphere, which form a waveguide commonly known as the Earth-ionosphere waveguide (EIWG). Therefore, propagating VLF/LF signals carry with them information about the current state of the *D* region. Because of this global propagation and since waves are able to penetrate significantly into water via the skin effect, various navies have constructed and operated VLF transmitters for the purposes of submarine communications. These transmitters operate almost continuously at constant power and frequency allowing an observer to employ them to monitor the current conditions of the ionosphere. For example, McRae and Thomson (2000), Thomson (1993), Thomson et al. (2007), & Thomson and McRae (2009), and Thomson (2010) have all used these VLF transmitters to infer the ionospheric conditions for VLF propagation. In many VLF remote sensing studies, the *D* region is assumed to follow a two-parameter electron density profile consisting of a height h' and a steepness β, as introduced by Wait and Spies (1964). A propagation model such as the long wavelength propagation capability (LWPC) code (Ferguson, 1998) is then used to estimate ionospheric waveguide parameters that most closely match observations. Many have used VLF transmitters and LWPC to infer simplified ionospheric parameters during solar flares (Dahlgren et al., 2011; Grubor et al., 2008; Kolarski & Grubor, 2014; McRae & Thomson, 2004; Singh et al., 2013; Šulić & Srećković, 2014; Thomson & Clilverd, 2001; Thomson et al., 2005). Current VLF remote sensing techniques nearly always use this approach.

Large current sources in lightning flashes also generate powerful impulsive broadband radio wave packets in the VLF/LF bands known as "radio atmospherics" or "sferics." These sferics also propagate efficiently (few dB per Mm attenuation) to global distances guided by the EIWG. Sferics therefore provide a convenient signal of opportunity to monitor ionospheric conditions along the path from the lightning source to a VLF/LF receiver. Using this capability, Cummer et al. (1998) and Cheng et al. (2006) developed a technique of monitoring the modal interference pattern in sferic amplitude spectra to infer the Wait and Spies parameters. The observations were interpreted using a finite-difference time domain simulation, leading to estimates of midlatitude diurnal variations in the *D* region height h' and sharpness β (Han & Cummer, 2010a, 2010b; Han et al., 2011). For both VLF transmitter and sferic-based ionospheric remote sensing at large distances, the inferred *D* region waveguide parameters can be assumed to be a path-averaged inference, being the summation of multiple waveguide modes, except in the presence of a sharp scattering feature such as an early/fast event (Inan et al., 2010).

Using time domain sferics, Lay & Shao (2011a, 2011b) developed a technique to sense a small portion of the *D* region corresponding to the Fresnel refraction zone, or the region of the first ionospheric hop, and observed ionospheric disturbances in the effective reflection height and reflection loss. Combining the experimental observations with the modeling technique developed by Shao and Jacobson (2009), Shao et al. (2013), and Lay et al. (2014) inferred the Volland electron density parameterization (Volland, 1995), and h', β, respectively, in the Fresnel refraction zone allowing for a small spatial measurement. Recently, Carvalho et al. (2017) looked at change in effective height using a cross-correlation technique for lightning sources characterized at the International Center for Lightning Research and Testing.

The current literature using sferic-based ionospheric remote sensing techniques all utilizes key features of sferics implying applicability in specific source-receiver geometries. In contrast, the technique described in this work relaxes this requirement and therefore will allow for general applicability for sferic-based work. Furthermore, all prior sferic-based studies use only the azimuthal magnetic field ($B\phi$) or the vertical electric field (Ez). In this paper we describe a generalized technique to recover stable sferics with both azimuthal and radial magnetic fields ($B\phi$ and Br) for any source-receiver geometry, including time domain sferics, amplitude, and phase frequency spectra. This technique extends the usable frequency range to higher frequencies (the examples in this work use up to 50 kHz but even higher frequencies may be useful in general), where VLF/LF propagation is even more sensitive to ionospheric changes. This allows sensitivity to higher altitudes since higher frequency waves are able to penetrate further into the *D* region.

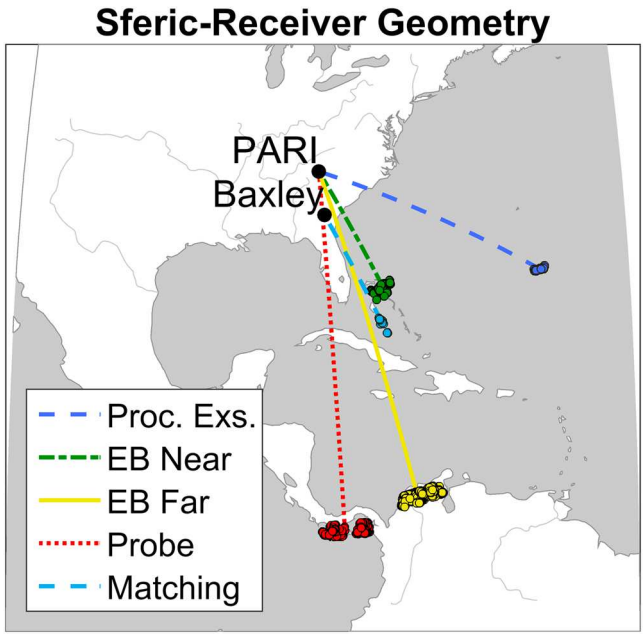

Figure 1. Map of all lightning regions selected. Very low frequency/low-frequency sferic propagation paths to PARI or Baxley are shown as lines. The colored dots indicate lightning stroke locations. Further information about lightning is given in Table 1.

With the more generalized sferic processing technique described here, as long as sferics are significantly higher than the background noise (signal-to-noise ratio (SNR) of >5 for this work), the full availability of lightning data from one or more lightning location networks can be used with an arbitrary receiver network. Lightning flashes occur about 40–50 times per second throughout the Earth (Christian et al., 2003). An average of 600–700 lightning storms occur each day with a mean duration of ~15 min (Hutchins et al., 2014) creating a global time-varying distribution of lightning-generated VLF/LF sources with ~57% of these sferics being measured at greater than our SNR threshold of 5. There is an opportunity to utilize this large data set of natural lightning emissions and an arbitrary receiver network for large-scale to global ionospheric *D* region characterization. The extent of the ionospheric coverage is proportional to the number of lightning strokes and their locations as well as the placement of utilized receivers. In this paper, we introduce the analysis tools needed to eventually expand sferic-based ionospheric remote sensing into a potentially global measurement. We present a method to simulate the VLF/LF emissions of broadband sferics with LWPC and use a forward modeling technique to match to the processed results. We discuss potential methods to utilize a large number of path-averaged *D* Region ionospheric inferences.

2. Data Description

We utilize VLF/LF (~1–50 kHz) magnetic field data sampled by an instrument similar to the AWESOME receiver described by Cohen et al. (2010). Two wire loops are mounted in the north/south (N/S) and east/west (E/W)

Table 1
Information on Lightning Regions Used in This Study

Lightning region	Date	Center time	Strokes	Size (km)	Receiver
Processing examples	21-Aug 2015	19:15:00 UT	214	103	PARI
Near error bars	1–15 Sep 2015	19:52:30 UT	14–368	12–187	PARI
Far error bars	1–15 Sep 2015	20:52:30 UT	14–1,430	28–418	PARI
Ionospheric probe	21-Aug 2015	Figure 12	68–1,193	129–426	PARI
Matching example	7-Aug 2016	15:48:20 UT	31 and 34	43 and 149	Baxley
Solar example	7-Aug 2016	Figure 17	34	149	Baxley

Note. Some figures utilize multiple dates and/or bins; for those studies the range information is given.

directions to capture both horizontal magnetic field components. The raw magnetic field data signal is first amplified then low-pass filtered with 470 kHz cutoff frequency to prevent aliasing. The signal is then sampled continuously at 1 MHz with 16-bit resolution and sensitivity of 0.03 – 0.1 fT/rt-Hz, depending on the size of the antenna. Next, the collected data are time synchronized to a GPS reference for an absolute time accuracy of 15 – 20 ns. All of the data used in this work are from receivers at Pisgah Astronomical Research Institute near Rosman, NC, United States (N35.1996, W82.8718) and Baxley, GA, United States (N31.8767, W82.3620). The locations of these site are shown in Figure 1 along with the lightning regions utilized in this study and the path from the regions to the relevant receiver.

We utilize lightning location data from the GLD360 network operated by Vaisala Inc., GLD360, whose basic operating principles are described in Said et al. (2010, 2013). It utilizes a combination of time of arrival, sferic shape, and a network of AWESOME VLF receivers (as described by Cohen et al., 2010) to geolocate lightning. GLD360 detects lightning with a global cloud-to-ground flash detection efficiency greater than 70% and reports peak current estimates, polarity, location, and time of occurrence for each lightning event. The location accuracy is estimated to be 1 – 4 km.

GLD360 does not distinguish between intracloud (IC) and cloud-to-ground (CG) strokes whose current sources differ significantly. Therefore, to further increase the integrity of processed sferics, we only use sferics greater than 10 kA in magnitude. This cutoff works to deselect IC strokes since they tend to be reported as low peak current events by the network (Cummins & Murphy, 2009).

In addition to CG/IC events lightning detection networks occasionally observe highly energetic and short pulses known as narrow bipolar events (Le Vine, 1980) or newly discovered energetic in-cloud pulses (Lyu et al., 2015) and label them as very high peak current IC strokes. Utilizing five receivers, Lyu et al. (2015) found and classified merely 139 narrow bipolar events/energetic in-cloud pulses over a period of 44 days. Therefore, we do not screen out these events from our data set.

3. Methods

The sferic waveform changes as a function of return stroke current parameters, but more dominantly as a function of distance and propagation conditions, namely, the ionospheric conditions along the path, as shown by Said et al. (2010).

In principle, one could do ionospheric remote sensing with an individual sferic, but this has shortcomings. First, the single sferic must have high SNR, which is often not the case for sferics from distant thunderstorms. Second, source variability will have a significant impact on the shape of an individual sferic. For these reasons, it is advantageous to take many sferics with the same propagation path and sum them up, both to increase the SNR and to mitigate varying source current and geometry.

Unfortunately, the uncertainty of propagation conditions by time and location contribute significantly to errors in lightning location estimates by networks such as GLD360. In turn, this error makes a straightforward time alignment of many sferics difficult since error in timing and location translate into timing uncertainty of the sferic waveforms that we call "jitter," even when the sferics have nearly the same propagation path. For example, assuming the speed of light propagation, 1 μs of jitter could be simply 1 μs in timing error, 300 m of location error, or likely an unknown combination of both. We demonstrate the effects of inherent jitter in Figure 2. We show a superposition of 214 sferics in gray over a period of 15 min, all originating from the cluster of blue dots in Figure 1 (each dot indicates a lightning stroke). For each stroke, its precise time and location as estimated by GLD360 is used to infer the arrival time of the sferic, which, assuming speed of light propagation, corresponds to $t = 0$. We also refer to this time as d/c, where d is the source-to-receiver distance. In Figure 2a, it is evident that there is significant jitter and waveform variation. In this example, the time-alignment standard deviation is 14 μs. The black curve represents the mean of all the sferics, which does not accurately capture the average shape due to the degraded time alignment and variation in sferic magnitude. Figures 2b and 2c show the same set of sferics after two critical steps in the sferic processing and time-alignment technique described in section 3.1.2. Following processing, we observe a significant improvement in the quality of the averaged sferic. In the remainder of this section, we detail how this is achieved.

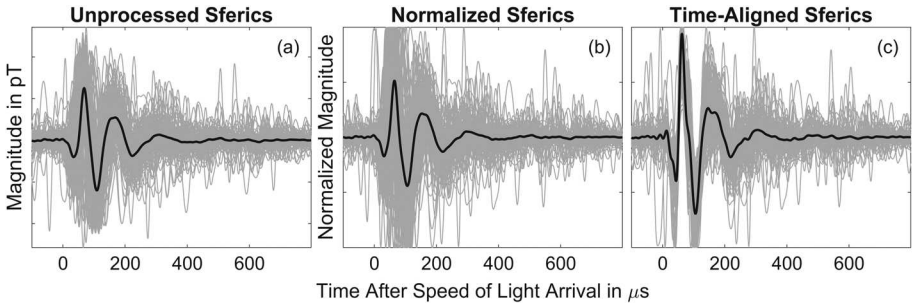

Figure 2. Example of the timing and location-induced timing jitter and its effect on sferic processing. Two hundred fourteen sferics from lightning events plotted as blue dots in Figure 1 are plotted as gray curves representing individual lightning strokes for unprocessed raw sferics (a), normalized sferics (b), and time-aligned sferics (c). The black curves represent the respective arithmetic mean.

3.1. Time Domain Sferics

Our goal is to time-align sferics in order to mitigate the effects of arrival time jitter as previously discussed, so we begin with processing in the time domain. Later, we will describe frequency domain techniques. The block diagram depicting our approach is given in Figure 3.

3.1.1. Narrowband Transmitter Removal

The two dominant sources of energy in the VLF/LF frequency band are lightning-generated sferics and communications transmitters (Chrissan & Fraser-Smith, 1996). These transmitters are used, for instance, by the U.S. Navy at high power with a very narrow bandwidth for submarine communications. To mitigate this "interference" source and improve the underlying sferic waveforms, we estimate and subtract the transmitters recorded by our receivers.

We first demodulate each VLF Minimum Shift Keying (MSK) signal as described in Gross et al. (2018). Next, we reconstruct each transmitter and subtract from the time series data. We observe a significant improvement in sferic quality over frequency spectra usually dominated by these transmitters, allowing recovery of underlying sferic information. The transmitters removed from the broadband data are detailed in Table 2. We demonstrate typical results by showing a sferic and frequency amplitude before and after narrowband removal in Figure 4.

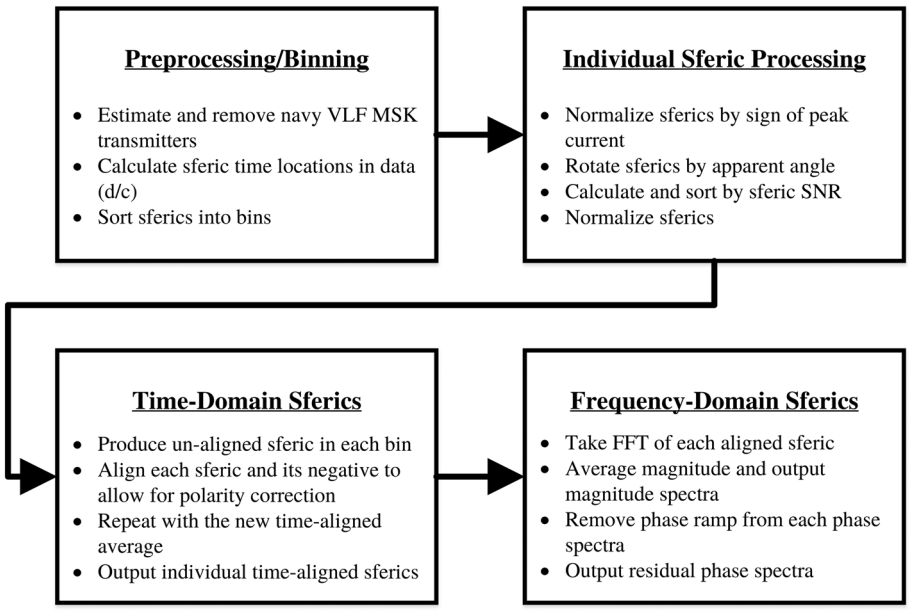

Figure 3. Block diagram of broadband sferic processing steps. Boxes group similar operations and each bullet represents an individual step. VLF=very low frequency; SNR=signal-to-noise ratio; FFT=fast Fourier transform.

Table 2
Transmitters Subtracted From Broadband Data

Location of transmitter	Call sign	Frequency (kHz)	Removed from
Rosnay, France	HWU	18.3	PARI/Baxley
Anthorn, UK	GBZ	19.6	PARI/Baxley
Exmouth, Australia	NWC	19.8	PARI/Baxley
Tavolara, Italy	ICV	20.27	PARI/Baxley
Lualuahei, HI	NPM	21.4	PARI/Baxley
Shelton, UK	GQD	22.1	PARI/Baxley
Rhauderfehn, Germany	DHO	23.4	PARI/Baxley
Cutler, ME	NAA	24.0	PARI/Baxley
Jim Creek, WA	NLK	24.8	PARI/Baxley
La Moure, ND	NML	25.2	PARI/Baxley
Aguada, Puerto Rico	NAU	40.75	PARI/Baxley

The transmitters can be clearly seen in Figure 4d as very strong but narrow frequency band signals. The results showing the same spectra after notch filtering and subtraction are displayed in Figures 4e and 4f. After removal of the transmitters, sferic information in the same frequency range as the transmitters can now be utilized in ionospheric remote sensing studies. This result is in contrast to the notch filtering results which subtract more than the transmitter energy, removing portions of the spectra from usability. A raw time domain sferic example is shown in Figure 4a, with the same sferic after notch filtering/MSK subtraction in Figures 4b and 4c. The example sferic SNR as described in Figure 7 and accompanying text improves from 2.2 to 5.9 with this technique while also recovering the underlying sferic spectrum.

We now evaluate the general performance of the coherent MSK removal algorithm compared to applying a simple notch filter. In the following analysis, the interference signal is a 1 s recording of an MSK transmitter with a high SNR, filtered over a 400 Hz bandwidth. The signal of interest is an impulse with a 2 kHz bandwidth centered on the transmitter. The results below indicate an upper bound on the performance difference between the coherent and notch filtering approaches, since in practice the impulsive signals will have a much larger bandwidth.

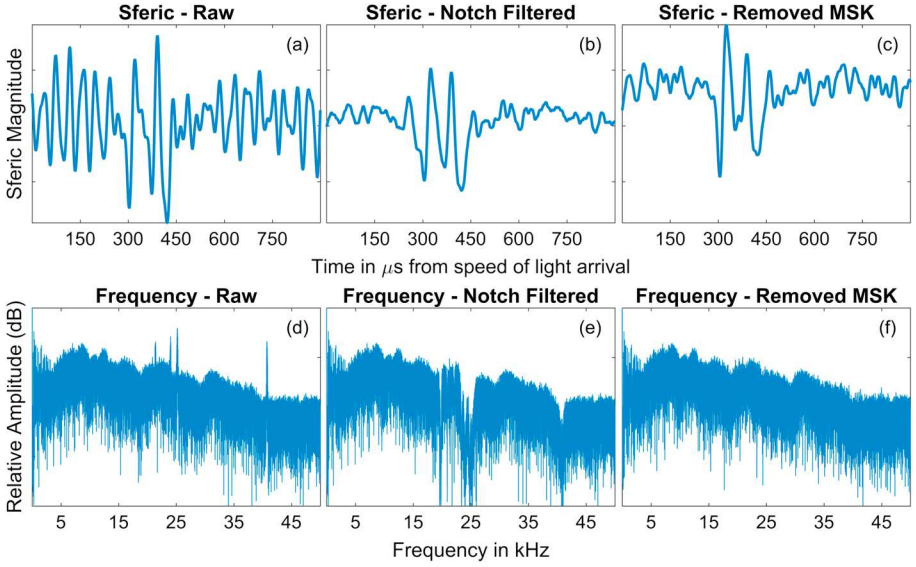

Figure 4. An example of coherent MSK signal subtraction. A time sferic and broadband spectra are shown for the raw data (a,d), notch filtered data (b,e), and the MSK subtracted data (c,f).

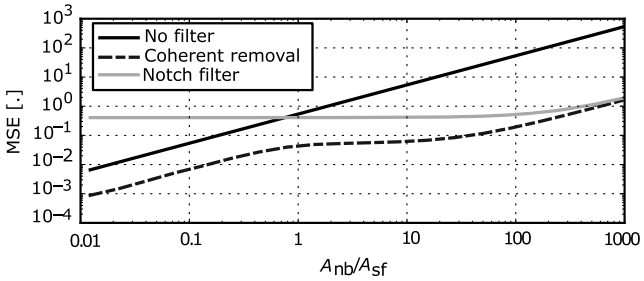

Figure 5. Mean-square error (MSE) of the recovered impulse as a function of narrowband amplitude normalized to the peak amplitude of the original impulse A_{sf}. The MSE is evaluated for three narrowband removal techniques: no filter (solid black line), 600 Hz notch filter (gray line), and coherent MSK removal (dashed line).

The performance of the coherent MSK subtraction technique can be quantified by the mean squared error (MSE) between the recovered impulse $\hat{x}_s(t)$ and the original impulse $x_s(t)$. Using a 200 μs integration window centered on the impulse time t_0 gives

$$\mathrm{MSE} = \frac{1}{200\ \mu\mathrm{s}} \int_{t_0-100\mu\mathrm{s}}^{t_0+100\mu\mathrm{s}} \left[\hat{x}_s(t) - x_s(t)\right]^2 \mathrm{d}t \equiv \| \hat{x}_s - x_s \|^2 \quad (1)$$

If we write the original narrowband transmitter signal as x_{nb} and the recovered transmitter signal as $\hat{x}_{nb}$, then $\hat{x}_s = (x_s + x_{nb}) - \hat{x}_{nb}$, and so the MSE can also be written as $\| x_{nb} - \hat{x}_{nb} \|^2$. That is, the MSE of the signal of interest is equivalent to the MSE of the reconstructed MSK signal compared to the original MSK signal.

Figure 5 plots the MSE of the recovered impulse using the coherent removal technique. For reference, the figure also shows the MSE with no filtering, and using a notch filter with 600 Hz bandwidth. The notch filter effectively removes both the narrowband transmitter and the in-band energy of the impulse. Thus, the MSE using a notch filter is relatively insensitive to the narrowband amplitude for modest narrowband amplitudes. For large amplitudes, evidently the notch filter attenuation outside the pass band is insufficient and the performance degrades slightly.

Across all narrowband magnitudes, the coherent removal technique outperforms the notch filtering. For weak narrowband signals, where $A_{nb} \lesssim A_{sf}$, the notch filter performs worse than applying no filter, since it removes both the (weak) narrowband signal and the energy of the impulse in that band. In contrast, for weak narrowband amplitudes the coherent removal approach reduces the MSE over the unfiltered case by nearly a factor of 10. For larger narrowband amplitudes, using a notch filter improves the MSE compared to the unfiltered case. Coherently demodulating and removing the narrowband signal, however, still outperforms notch filtering in this regime, since less energy in the impulse is removed. As the narrowband signal strength increases, the relative improvement of the coherent subtraction technique compared to notch filtering decreases, due to limits from the various filtering operations involved in the coherent subtraction technique.

3.1.2. Binning and Individual Sferic Processing

We begin sferic processing by taking the GLD360 location and timing estimate. Assuming the speed of light propagation delay, the propagation time from source to receiver is calculated and added to the reported time of the lightning stroke. We have empirically determined that the bulk of the sferic energy is captured in the first 700 μs after the speed of light arrival time (d/c).

As an example, we will utilize a set of lightning strokes depicted with blue dots in Figure 1. This thunderstorm consists of 358 reported strokes occurring between 19:07.5 and 19:22.5 UT on 21 August 2015, all within 90 km of each other. The utilized GLD360-inferred peak currents were as high as 295 kA. We have excluded 106 strokes that were below 10 kA, as these are more likely to have been IC strokes.

The receiver has two orthogonally oriented antennas that measure the N/S and E/W components of the incident sferic's magnetic field. We next rotate the two-channel data to maximize the total energy on one channel while minimizing it on the other. The N/S and E/W components are shown in Figures 6a and 6c. We digitally rotate the two channels to maximize the total energy on one channel over the period of 100 μs before d/c and 1,100 μs after d/c producing a high-SNR and a low-SNR channel plotted in Figures 6b and 6d. With no induced scattering along the source-receiver path, this is the same as rotating so that the high-SNR channel measured the perpendicular magnetic field or Bϕ, while the low-SNR channel measures the radial magnetic field or Br.

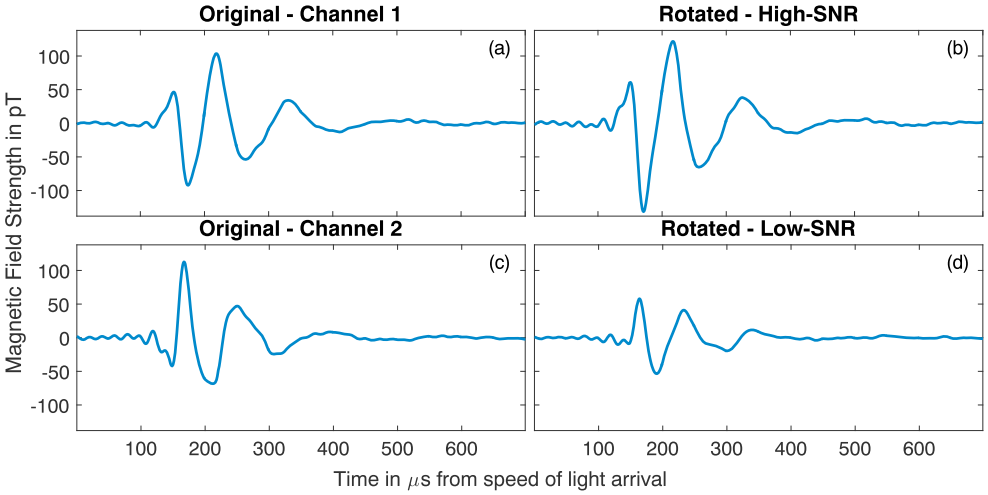

Figure 6. An example of digital rotation of a sferic. (a,c) Channels 1 and 2 before rotation. (b,d) Channels 1 and 2 after rotation known as "High-SNR" and "Low-SNR" or Bϕ and Br, respectively. SNR=signal-to-noise ratio.

This is because the attenuation of Br is significantly higher than Bϕ. It is worth noting that the direction of rotation is not necessarily the same direction as the source from the antenna. The discrepancy is likely due to site-dependent scattering and induction that modifies the apparent angle-of-arrival due to buried power lines or mountains (see Said, 2009, p. 93; Zoghzoghy, 2015, p. 45). It is also significant that because VLF sferics are not perfectly linearly polarized, the low-SNR channel still has a detectable magnetic field which can be recovered with this technique, not yet utilized in former sferic studies. Recent results from Gross et al. (2018) utilize phase and amplitude of both Bϕ and Br of narrowband VLF signals to develop a polarization ellipse method to monitor the *D* Region and diagnose ionospheric perturbations, with advantages over previous narrowband studies. Similarly, amplitude and phase of both Bϕ and Br of broadband sferics recovered in this study may reveal or clarify information on the *D* Region and related phenomena.

For lightning strokes occurring in a small time and location range, propagation conditions are very similar. We therefore bin the strokes in space and time so that we can apply a superposed epoch analysis to arrive at an average or "representative" sferic for each path at each time. We ignore bins that have a count of less than 10 strokes. By averaging, we are mitigating the effect of lightning source parameter variability, since these would otherwise make successive strokes from the same storm look very different (see, e.g., Figure 11). After the sferics are binned together they are multiplied by their polarity (as detected by GLD360) so that all positive and negative strokes do not destructively cancel.

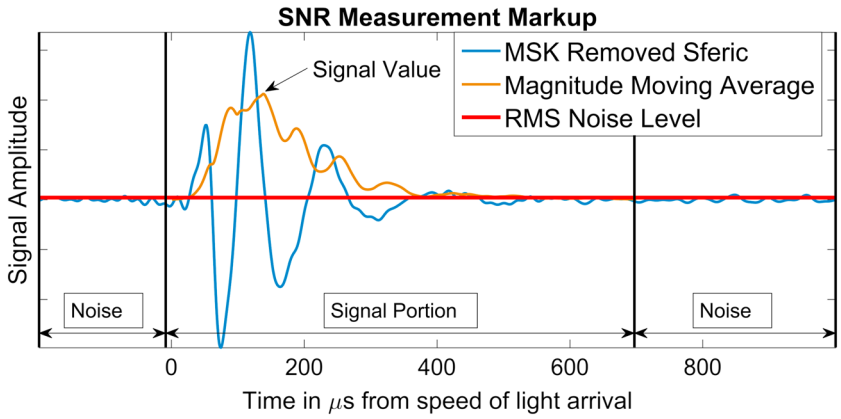

Figure 7. An illustration of signal-to-noise ratio (SNR) calculation. The sferic appears in blue in the "Signal Portion." The red line represents the root-mean-square (RMS) of ambient noise on the channel. The yellow line is the moving average filtered portion of the signal.

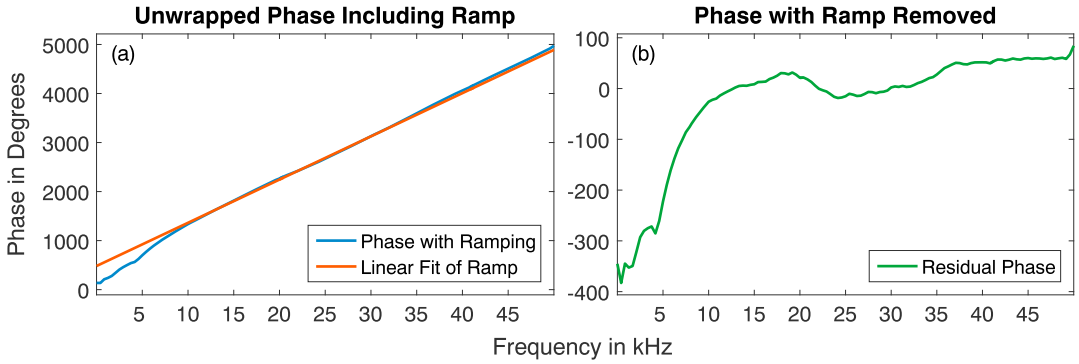

Figure 8. Removal of phase ramping. (a) The blue signal is a single sferic unwrapped phase with a 180° reference and the red line is the linear fit between 9 and 30 kHz interpolated for the rest of the signal. (b) The residual phase or the measured phase subtracted by the linear fit. This linear phase adjustment is similar to the technique used by Dowden et al. (2002) to estimate time of arrival in a lightning geolocation application, differing from the purpose here to calculate the Bϕ residual phase.

We thus arrive at a representative sferic which is made up of all the sferics within that bin. Unfortunately, this result may be distorted by low-SNR sferics and by the timing jitter of received sferics as previously discussed. Therefore, we automatically deselect these low-SNR outliers. The SNR is calculated as follows and demonstrated in Figure 7. We first smooth the sferic, shown in blue, by applying a moving average with a window size of 40 μs, the result of which is shown in orange. The peak value of this moving average is taken to be the signal value, as indicated by the arrow. To calculate the noise level, we find the root-mean-square value of two concatenated signal portions, the first starting 200 μs before d/c until d/c and the second starting 700 μs after d/c until 1,000 μs after d/c, shown by the red trace. Sferics with an SNR of less than 5 (or 7 dB) are removed for all of the examples in this paper.

Having now removed the low-SNR sferics, we now equally weight the remaining sferics. We normalize all sferics by the maximum of their absolute value. This ensures that the averaging technique is not dominated by a small number of particularly intense sferics and effectively normalizes all sferics to have the same intensity. We are now ready to take a straight arithmetic average of the remaining normalized sferics, the result of which is the sferic shown Figure 2b. This representative sferic is improved from the initial sferic, but the subsequent processing steps will improve the SNR even further.

We now consider removal of the timing jitter, in order to align all the sferics in each bin. We do this recursively. First, a raw average is taken of all of the sferics within a bin with no adjustment to the sferic jitter. Then, each sferic within that bin is aligned to the raw average by finding the maximum cross correlation between the two. This cross correlation is performed for both the raw sferic and a flipped (i.e., multiplied by −1) version of the raw sferic, accounting for the possibility of a polarity error in the GLD360 estimate. The highest cross-correlation location is calculated using the upsampled sferic so that the smallest adjustment possible is 1 μs, and the sferic is delayed or advanced by the amount required to move this delay to 0. A new arithmetic average is taken with the aligned (and possibly flipped) sferics. We continue this process iteratively until convergence occurs (typically approximately 3 to 5 steps). After convergence, the final time domain output is the average of the aligned sferics. The final time-aligned sferics and time domain output are shown in Figure 2c.

3.2. Frequency Domain Sferics

Past studies have utilized the spectral interference pattern for ionospheric sensing (Cheng et al., 2006; Cummer et al., 1998; Han & Cummer, 2010a, 2010b). These studies used modal interference patterns observed in sferic spectra, which is primarily a propagation effect, making their techniques independent of lightning source parameters. Another advantage of frequency domain analysis is that the amplitude spectra is insensitive to timing jitter.

Having finished normalizing and time-aligning sferics in the time domain, we now consider how to extract a reliable amplitude and phase spectra for the average sferic. Deriving the amplitude spectra of the representative waveform is straightforward, we take the fast Fourier transform (FFT) of each sferic within a bin, and then take the mean of magnitude of the FFT coefficients of each sferic.

However, in order to recover stable phase spectra an additional step is necessary. The FFT's $t = 0$ reference is the beginning of the input signal, or d/c. Since the VLF/LF group velocity is slower than the speed of light reference chosen in this work, the sferic arrives after the d/c, so there is a time delay built into the signal. In the frequency domain, this is equivalent to multiplying the Fourier transform by a complex exponential linearly proportional to the time delay $e^{i\cdot 2\pi\cdot f\cdot t_{\text{delay}}}$. The complex exponential adds a "ramp" to the phase frequency curve, with the slope proportional to the time delay. We refer to this feature as phase ramping, equivalent to a small residual delay. Any small timing jitter still present in the time domain sferics will manifest itself as an additional phase ramping. Because of the sensitivity of phase spectra to very small timing errors, we calculate and output a residual phase by removing all phase ramping. The phase ramp removed by this technique corresponds to a removal of the linear group delay that depends on distance and an additional time adjustment of at 10s of μs.

Since phase wraps around and repeats every 360°, each signal is then unwrapped with a 180° reference resulting in the raw phase. This results in a waveform similar blue Bϕ phase sferic in Figure 8a. A best fit linear trend is calculated between 9 and 30 kHz of the Bϕ component, the portion of the signal we empirically determined to be the highest-SNR portion of the signal. This linear fit is removed from the unwrapped phase of the Bϕ and B*r* signals, and what remains are the residual phases, as shown for the Bϕ signal in of Figure 8b. The final residual phase spectrum is the average of the residual phase of each sferic within a bin. Importantly, this result is now insensitive to even small timing jitter. One can view this as fine-scale timing adjustment, with course adjustments having been done in the time domain stage of the analysis.

4. Results

4.1. Processing Outputs

In order to quantify the effectiveness of this technique, we measure sferic variability for two examples in order to arrive at measurement error bars. We focus on daytime cases, where the *D* region ionosphere is known to be steady and fairly predictable in the absence of a solar flare event (Thomson, 1993). We select a 15 day period from 1 to 15 September 2015, of which 9 days had a significant amount of lightning in the same location near the Bahamas, as shown/detailed in Figure 1/Table 1. We then calculate the average sferic for the same 15 min period of time, from 18:45 to 19:00 UT, in each day. For the 9 lightning days, their binned/processed time domain and amplitude/phase spectra of both magnetic field components are plotted in gray in Figure 9. The mean of the waveforms is plotted in black with some sample error bars around the mean in red, reflecting the variability of the result.

The described processing technique is generally applicable to sferics arriving from an arbitrary location and is only limited by the detectability of arriving sferics. To demonstrate this, we provide another example of error bar calculations from sferics from source lightning at region further from Pisgah Astronomical Research Institute, located near the northern border of Colombia/Venezuela (Figure 10) for the same date region and 20:45:00–21:00:00 UT of which all 15 were lightning days. The time domain, amplitude, and phase spectrum for both magnetic field components are shown again.

The recovered sferic waveforms for both magnetic field components follow the same temporal and spectral trends indicating the stability of the technique. In contrast, we plot 7 random sferics from one of the bins making up single representative sferic in Figure 9 (1 September 2015) that contains 547 sferics in Figure 11. The results for time domain and amplitude/phase spectral domain demonstrate the highly varied nature of individual sferics for both magnetic field components, in contrast to the results of Figures 9 and 10.

Examination of Geostationary Operational Environmental Satellite (GOES) X-ray data shows no solar flare on these 15 days, so the sferics should in principle be very repeatable over this period, due to the relative steadiness of the daytime *D* region ionosphere. The error bar calculation demonstrates the residual variation for the example geometry after our processing technique. The averaged time domain sferics still seem to "jitter" compared to each other since they will all be time shifted according to the built-in timing bias of the lightning location network. Therefore, for visual clarity the output time domain binned results are time aligned to each other before producing the error bars in both examples. These time domain results are very similar in both cases, with error bars increasing with relative sferic magnetic field strength for both components.

For both examples, the amplitude Bϕ error bars are smaller than B*r*, which is a reflection of the relatively low SNR of the B*r* channel; however, the B*r* sferics still follow a clear trend. For the shorter path, the error bars remain relatively steady across the sferic spectra. The Bϕ error bars from 5 to 48 kHz are between ~0.5

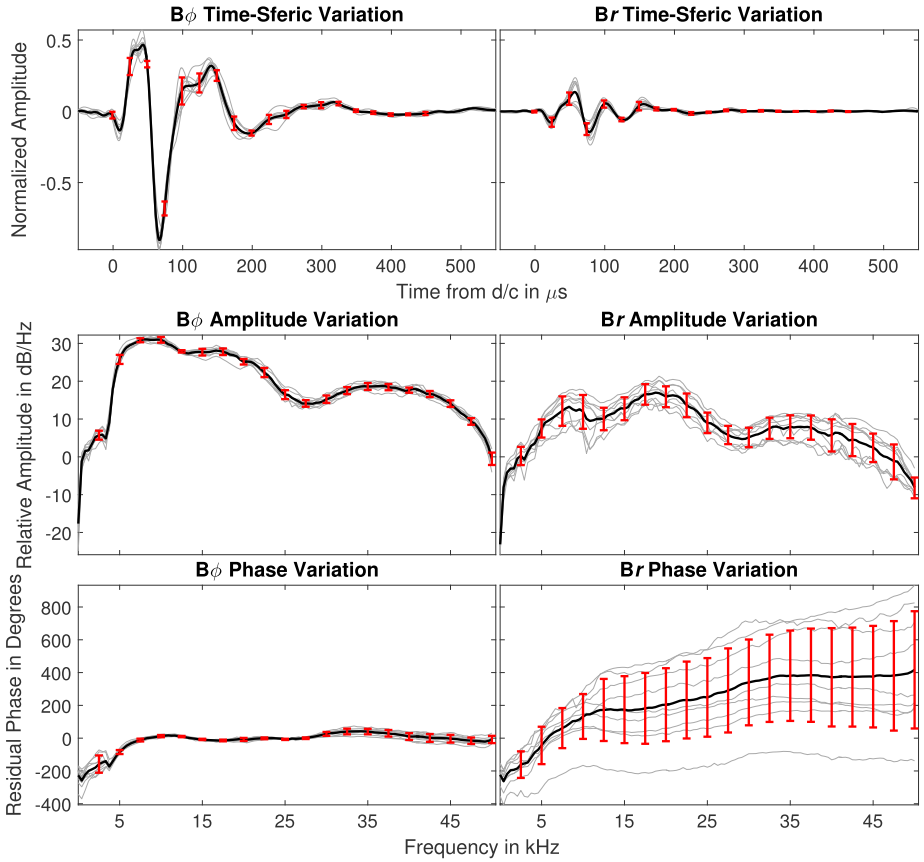

Figure 9. Illustration of calculated error bars for Bϕ and Br from 1 to 15 September 2015 and 18:45–19:00 UT. The source center to receiver distance is 1,150 km with further information for this example is given in Table 1 with the "Near Error Bars" label. Each available representative waveform is plotted in gray, the mean is plotted in black, and the linear standard deviation is represented each direction from the mean in red plotted at 2.5 kHz intervals. The strokes used in these examples are plotted in green in Figure 1.

and 1 dB, whereas the Br error bars are ~2–4 dB. The error bars for Bϕ phase are relatively uniform until nearly 30–35 kHz when the results begin to diverge slightly. The Bϕ spectral error bars are most stable from 5 to 30 kHz at ~5°. The error bars are very large in the Br phase component compared to Bϕ, this is because the phase offset adjustment is taken from the Bϕ component, so the offset and linear trend that differs between each result in Br phase is a physically meaningful result that may be obscured by a simple rendering of the error bars. Despite the large size of the error bars, the results follow similar trends.

For the longer path, spectral amplitude error bars are smaller for frequencies below 20 kHz in Bϕ compared to Br but converge to very similar values above 25 kHz. The Bϕ error bars are ~0.5 dB from 10 to 20 kHz, while they rise to ~1.5 dB for 30–49 kHz. Br amplitude bars are ~1.5 dB for nearly the entire processed spectrum (10–49 kHz). The phase spectral magnetic field components have similar trends to the near path results.

For both examples, nearly the entire frequency band is usable, as the error bars even at higher frequencies are fairly small compared to the general variability of sferics, as we show later in Figures 12 and 13, which may be caused by unknowable factors such as the varying geometry of individual stroke channels or meteorological differences of varying thundercloud structures. A small amount of the variability we report may be due to a gradual seasonal shift in the *D* region ionospheric conditions, but as we ignore this effect, our variability measurement represents an upper bound.

The results recently reported in Carvalho et al. (2017) argue the need to have well characterized source parameters for each lightning return stroke to be able to perform ionospheric inference. But this conclusion need only apply for the use of a single or a very small number of sferics. We know nothing precisely about the return stroke current or geometries of the channels used in this work, but it is clear careful use of many lightning

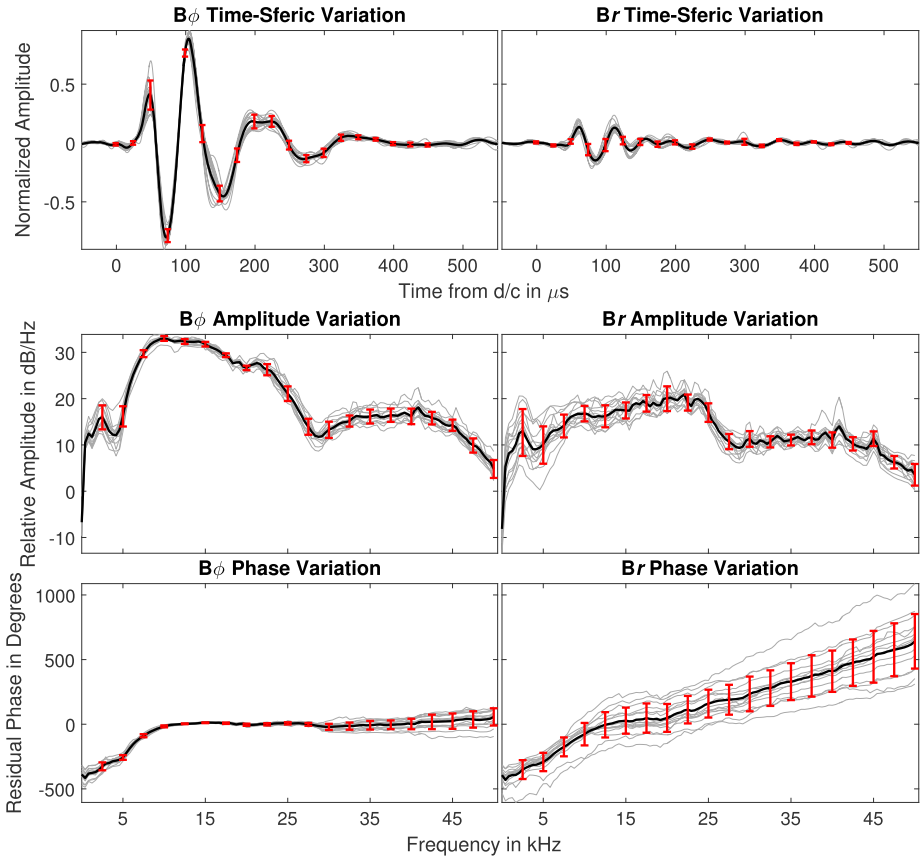

Figure 10. Illustration of calculated error bars for Bϕ and B*r* from 1 to 15 September 2015 and 20:45:00–21:00:00 UT. The source center to receiver distance is 2,900 km with further information for this example is given in Table 1 with the "Far Error Bars" label. Each available representative waveform is plotted in gray, the mean is plotted in black, and the linear standard deviation is represented each direction from the mean in red plotted at 2.5 kHz intervals. The strokes used in these examples are plotted in yellow in Figure 1.

strokes can be used to calculate a repeatable representative sferic waveforms, in spite of the natural variability of lightning source current and geometry. Full broadband information is now available with high fidelity, with widely distributed sources in space and time. This is true for time domain and amplitude/phase spectral sferics for both magnetic field components.

In principle, error bars like those shown in Figures 9 and 10 can be calculated for any path as long as there is enough lightning over a period of time to evaluate the measurement variability. Once the error bar is calculated, a sferic spectral feature that exceeds these bounds is likely due to changes in the ionospheric conditions. Hence, we now evaluate cases where the *D* region (and therefore the sferic spectra for a given path) are presumed to be different. Various ionospheric disturbances may affect sferic spectra differently, so the pattern of spectra changes may indicate the type of event. Figures 12 and 13 shows several sferic spectra measurements on 21 August 2015 for both Bϕ and B*r*, respectively. The strokes used in these examples are shown in red in Figure 1. The left-hand panels in Figures 12 and 13 show amplitude and phase for quiet solar conditions near local noon. Once again, the daytime sferic amplitude and phase spectra are highly repeatable and steady, reflecting the stability of both the *D* region and our analysis technique.

In the right-hand panels, sferics are shown for four very different ionospheric conditions: in particular, we show the sferic spectra during the nighttime (when the *D* region ionization is much lower), during sunset (when modal interference at the day/night terminator is important), and during a series of solar flares that commenced at 19:12 UT. The uniqueness of these waveforms compared to each other, taken with the stability of processing results for both Bϕ and B*r*, gives us the ability to discern different ionospheric conditions. With high-quality average sferic estimates in both time and amplitude/phase domains, we are able to develop

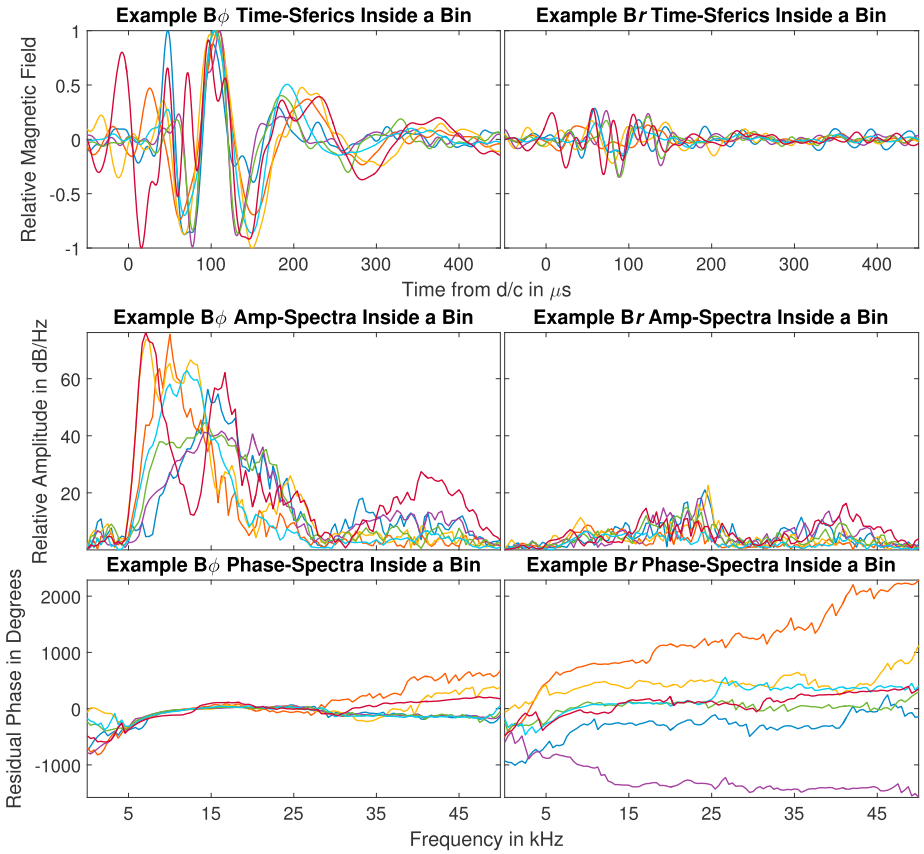

Figure 11. Example of individual sferics inside of a bin.

a generalized approach to ionospheric characterization with comparison to a numerical model described in section 4.2, not dependent on specific sferic features.

A typical CG lightning flash may include a first stroke and then (particularly for negative flashes) a number of subsequent strokes. It is known that first and subsequent strokes have different source characteristics (Rakov & Uman, 2003, Chapter 4.6). We therefore classified GLD360-reported lightning strokes as either a first or a subsequent stroke. A subsequent stroke was defined as having been geolocated within 100 m and within 100 μs after another stroke. We repeated the aforementioned analysis on only subsequent strokes, or only first strokes, and we observed no significant difference between their characteristics as observed with our technique. This underlies the fact that our analysis technique isolates ionospheric variability and minimizes the effect of lightning source variability (geometry and current waveform) while taking care of lightning location network-induced jitter.

4.2. Sferic Modeling

The bulk of energy received at VLF/LF frequencies are impulsively radiated during the return stroke of lightning. The measured return stroke current waveforms are typically unipolar with a faster rise than fall time. We utilize the traditional Bruce and Golde model of the channel base current (Bruce & Golde, 1941; Dennis & Pierce, 1964; Jones, 1970), which is a sum of two exponentials: $I(z = 0, t) = I_0[e^{-t/\tau_f} - e^{-t/\tau_r}]$. The return stroke travels up the channel from ground to the cloud base with propagation velocities of about 0.1 to 0.9**c**. The examples shown here use a return stroke velocity of $v_f = 0.75 \cdot \mathbf{c}$ and a channel height of $H = 3$ km. As the pulse travels, the magnitude is attenuated due to various loss mechanisms such as light (lightning) or heat/sound (thunder). This attenuation has well-matched propagation observations when the return stroke is modeled as a modified transmission line linear (MTLL) (see Rakov & Uman, 2003, for a broader discussion of return stroke modeling and lightning parameters). MTLL describes the channel current at height z and time t with respect to the channel base current by the following equation: $I(z, t) = u(t - z/v_f) \cdot (1 - z/H) \cdot I(0, t - z/v_f)$, where $u(\ldots)$ is the unit step function. For this work $\tau_r = 0.3\,\mu s$ and $\tau_f = 5\,\mu s$ which correspond to 10% to 90% rise and fall times of 0.45 μs and 10.7 μs, respectively.

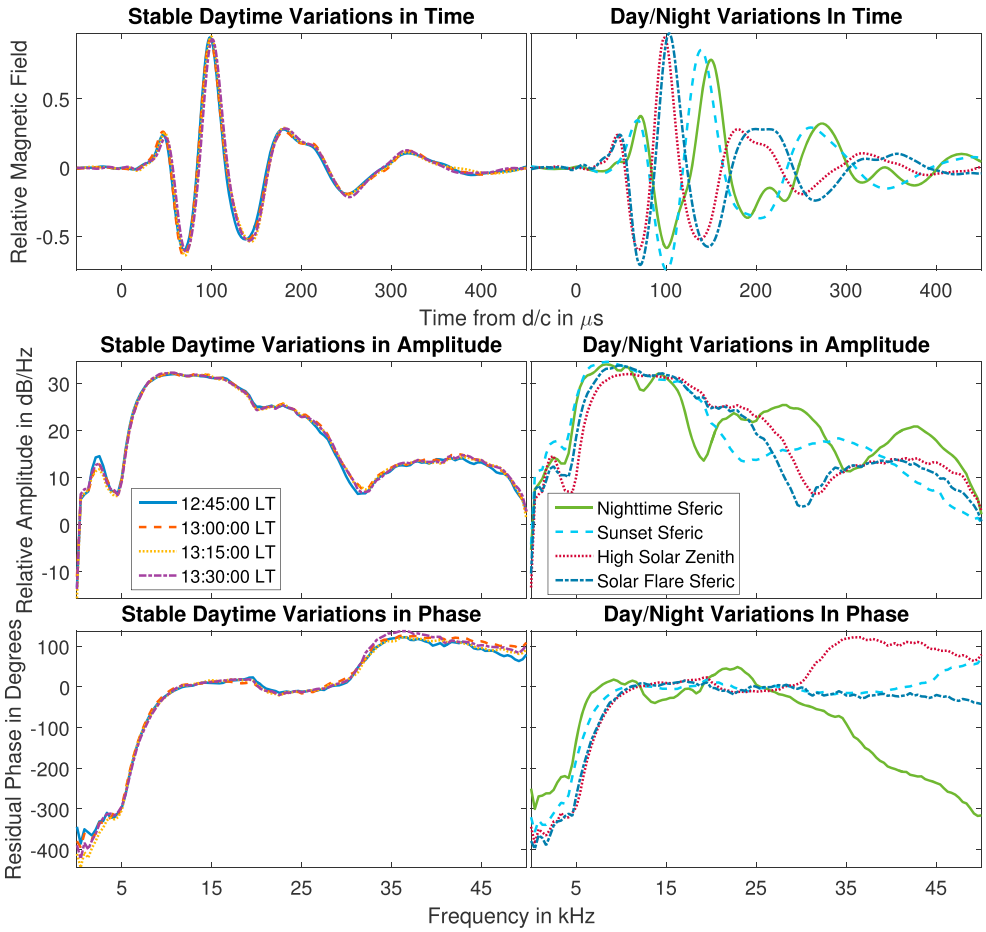

Figure 12. Example of processing stability for Bϕ and demonstration of detectability of variations in ionospheric structure on the test day of 21 August 2015. The center times of daytime sferics are given in the left legend. The center times of the nighttime, sunset, high solar zenith, and solar flare sferic are 06:15:00, 00:22:30, 16:45:00, and 22:15:00 UT, respectively.

The lightning channel is divided into six equal segments. The frequency components of the input current segments are calculated with the FFT.

LWPC takes the real EIWG parameters from a built-in lookup table, along with an assumed ionosphere, and simulates the amplitude and phase of a single frequency versus distance of the magnetic fields. If the sources are simulated to match the appropriate lightning channel segment, it can be seen as an input to the EIWG system. LWPC can be seen as the transfer function of the EIWG. Therefore the entire sferic can be simulated by taking the Fourier products of the LWPC results and the current frequency weights and summing up the contribution from each segment. This process is depicted in a cartoon in Figure 14.

We follow the Wait and Spies idea of electron density parametrization (Wait & Spies, 1964) with h' and β being interpreted as the effective D region height and sharpness, respectively. This parameterization can be expressed as

$$N_e(h) = 1.43 \times 10^7 \exp(-0.15h') \cdot \exp[(\beta - 0.15)(h - h')] \quad \text{cm}^{-3} \tag{2}$$

where h', is in km and β is in km^{-1}. By simulating h' and β over a wide parameter space, the simulation results can be compared directly to the measured sferic. The best match is interpreted as the real average electron density profile over the path, to the extent of the accuracy of LWPC and the parameterized assumption. As an example, a processed sferic during the daytime at Baxley is compared to the simulation results in Figures 15 and 16. The lightning strokes used in the following matching example occurred on 7 August 2016 from 15:43:20 to 15:53:20 UT and are shown in Figure 1 as light blue dots and described in Table 1

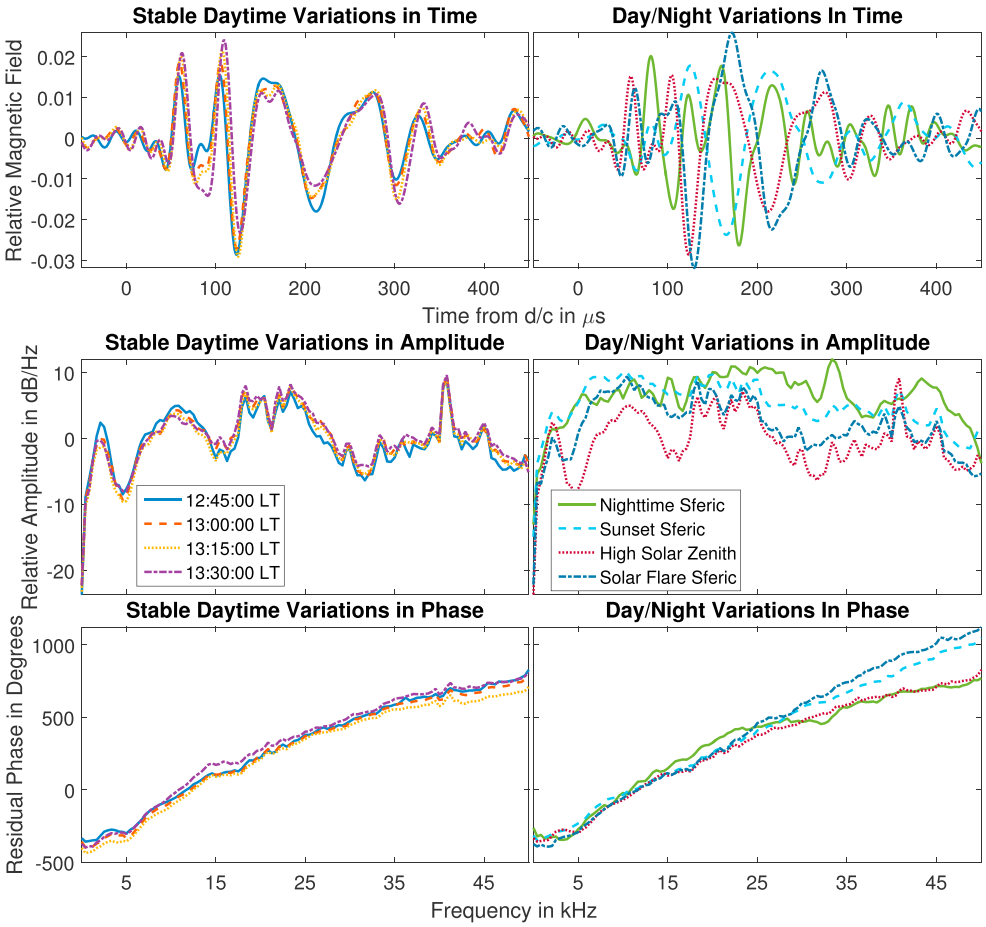

Figure 13. Example of processing stability for B*r* and demonstration of detectability of variations in ionospheric structure on the test day of 21 August 2015. The center times of daytime sferics are given in the left legend. The center times of the nighttime, sunset, high solar zenith, and solar flare sferic are 06:15:00, 00:22:30, 16:45:00, and 22:15:00 UT, respectively.

as "Matching Example." The processed sferic for this example is also utilized as the ambient "Ambient Measured Sferic" in Figure 17.

We determine the best fit by taking a $\ell 2$ norm of the difference of each simulated Bϕ sferic to a given processed sferic from 5 to 30 kHz for both log amplitude and phase over the entire simulated h' and β space. Next, we shift and normalize both log amplitude and phase so they vary between 0 and 1 weighting them the same in model matching. Lastly, we sum the min space from log amplitude and phase together and then normalize and shift, taking the smallest value to be the best fit. The contributing and summed spaces are plotted in Figure 15. In this example the best fit was determined to be $h' = 70$ km, and $\beta = 0.4$ km^{-1} which is plotted as a red dashed curve in Figure 16.

Due to runtime errors, the simulated spectrum below 5 kHz is excluded. Other examples marked as colored dots in Figure 15 varying h' and β, respectively, are included. The entire spectrum for both phase and amplitude change significantly when varying h' and β corresponding to increased $\ell 2$ norm values. For the given example the combined min space has a clear minimum with increasingly worse results as you move from the best fit. The normalized and raw $\ell 2$ norm values for the example simulation-measured sferic differences are given in Table 3.

For a 3 km change in h' or a 0.06 km^{-1} change in β the amplitude and phase scaled $\ell 2$ norm changes by a minimum of 100%. Consideration of frequencies above 30 kHz provides a significantly different answer and poorer broadband agreement which may indicate that the Wait and Spies h', β parametrization is not sufficient when considering higher frequencies which are sensitive to different electron densities, and in turn higher altitudes of the *D* region.

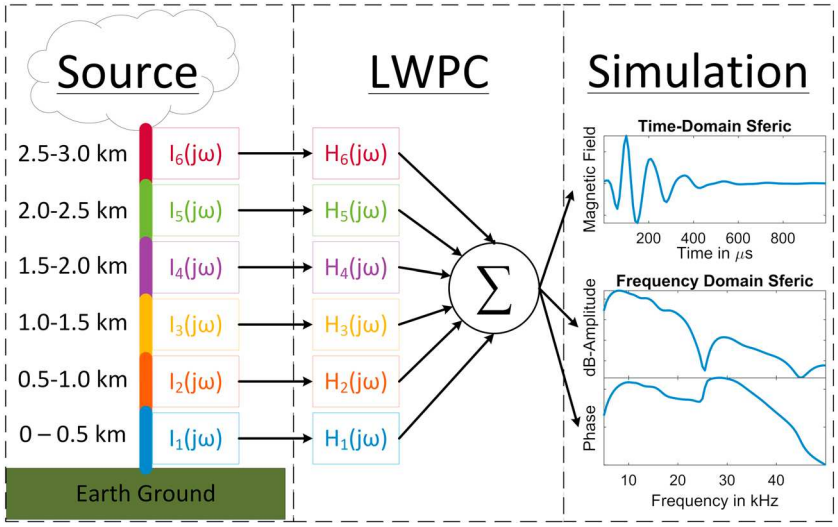

Figure 14. An illustration of described process to model a sferic. The colors indicate the height of certain segments and are labeled according to their altitude. The currents $I_n(j\omega)$ are defined according to the given parameters and equations, represented in the frequency domain. The transfer functions $H_n(j\omega)$ are calculated by long wavelength propagation capability (LWPC).

On 7 August 2016 two *X*-ray solar flares commenced: a M2 (2×10^{-5} W m^{-2}) at 14:30 UT and a C9 (9×10^{-6} W m^{-2}) at 15:04 UT . We consider the change in propagation conditions during the C9 flare and after it subsided. The lightning strokes used in the solar flare matching example occurred from 15:10:00–15:20:00 and 15:43:20–15:53:20 UT for the solar flare sferic and the ambient sferic, respectively. They are shown on Figure 1 as light blue dots and described in Table 1 as "Solar Example."

Figures 17a and 17c show the amplitude and phase for the Bϕ solar flare sferic. Figures 17b and 17d the Bϕ ambient sferic after the solar flares have dissipated. For visual comparison the best fit simulations for both sferics are shown in both cases with the $\ell 2$ norm matching values listed in Table 3. The sferic waveform has significantly changed as a result of the solar flare affecting the *D* region ionosphere. Similar to past work (e.g., Han & Cummer, 2010a), this solar flare caused a decrease in h', from 70 to 67 km, and an increase of β from 0.4 to 0.44 km^{-1}. The daytime h' and β inferences made in these examples agree with the inferences from Han and Cummer (2010a), Han et al. (2011), and related studies moreso than the results from Lay et al. (2014) and related studies.

The amplitude and phase for the ambient case and amplitude for the solar flare case are in good agreement with the best fit simulation as seen in Figures 17a, 17b, and 17d. However, the phase measurement differs significantly with the model during a solar flare (Figure 17c). This result differs from narrowband studies (e.g., McRae & Thomson, 2004) that consider phase with LWPC during a solar flare and find a good agreement.

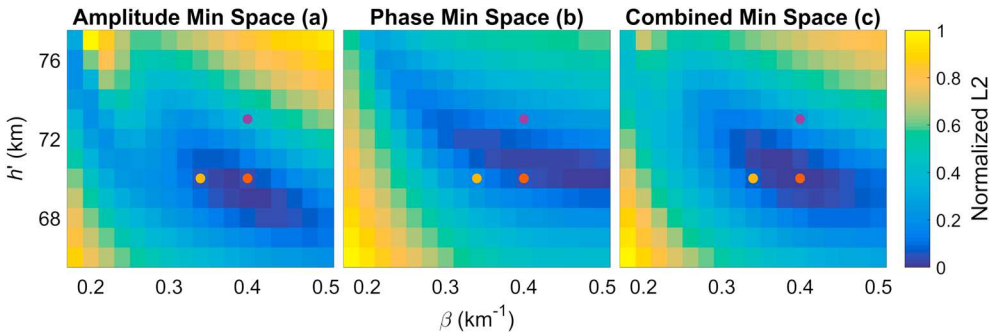

Figure 15. Normalized $\ell 2$ norm difference between simulations over h' versus β space and a processed sferic from Baxley for Bϕ amplitude (a), Bϕ phase (b), and Bϕ combined amplitude and phase (c). The colored circle markers correspond to the example simulations shown in Figure 16.

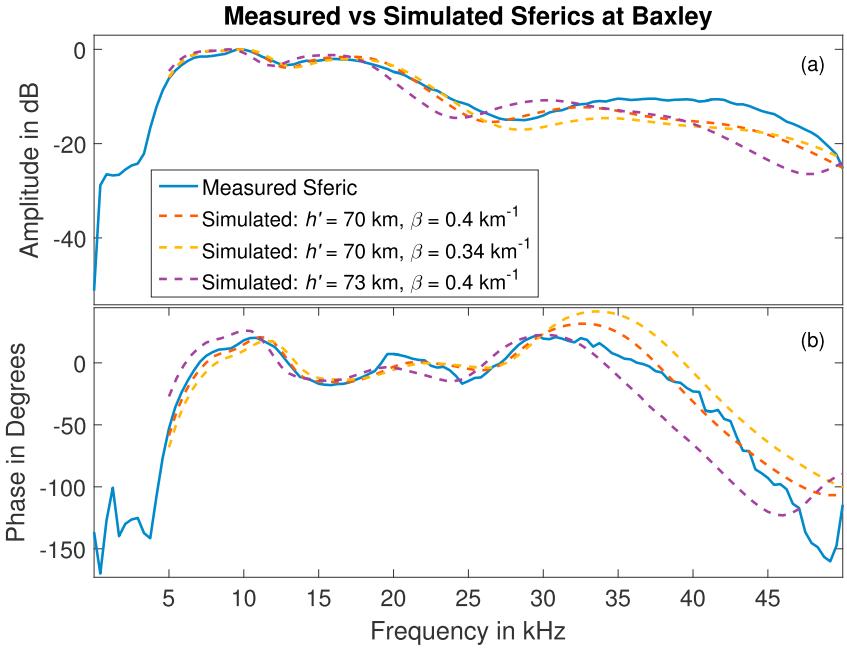

Figure 16. Comparison of a measured and processed Bϕ amplitude (a) and phase (b) sferic versus some simulations with assumed h' and β.

This could be explained by the fact that spectral residual phase values do have similar values at specific frequencies. However, the trend is not in common across the spectrum, a difference that cannot be resolved from a single narrowband transmitter-receiver path. It is possible the disagreement may be explained by the insufficiency of the Wait and Spies parametrization during a solar flare. In any case, it is clear that utilizing broadband amplitude and phase together may allow for greater understanding of solar flares and their effect on the *D* region ionosphere.

Morfitt (1977) and Ferguson and Snyder (1980) show that h' and β may have a frequency dependence that is more noticeable at nighttime. This may explain why a single h' and β estimate matches the measured spectra from ~5 to 30 kHz but divert at higher frequencies. The frequency dependence stems from the fact that the effective wave reflection height increases with frequency since the electron density increases with altitude,

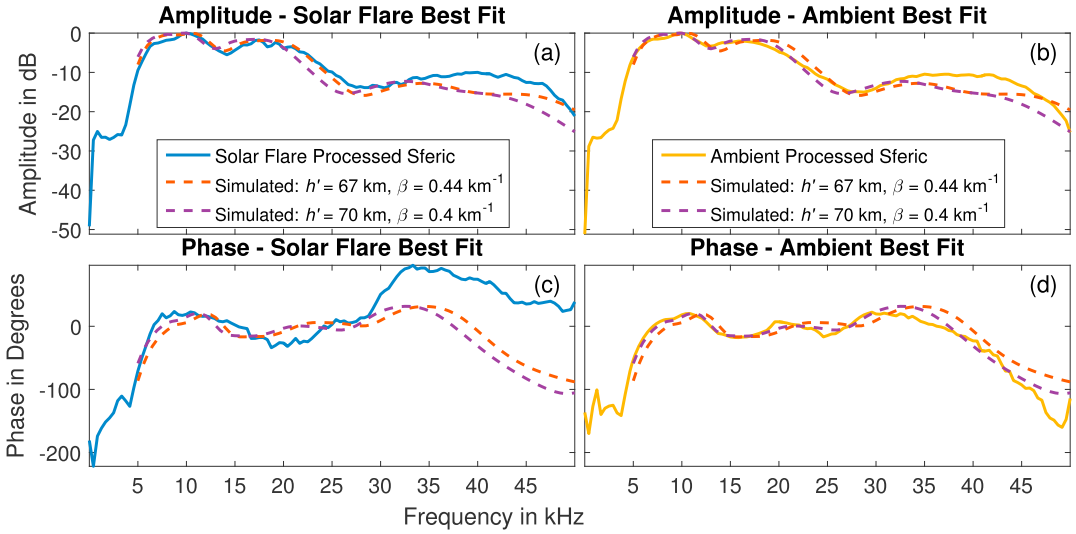

Figure 17. Comparison of processed sferics during (a,c) and after a solar flare (b,d). Best fit simulations of both cases are shown for amplitude and phase.

Table 3
ℓ^2 Norm Values for Matching Examples

Figure	h' (km)	β (km)$^{-1}$	Amplitude scaled	Phase scaled	Amplitude raw	Phase raw
16	70	0.40	0.03	0.06	7.5	36.9
16	70	0.34	0.06	0.16	8.2	62.3
16	73	0.40	0.39	0.19	17.3	70.1
17	70	0.40	0.04	0.17	9.1	135.6
17	67	0.44	0.03	0.06	7.5	36.9

which may not increase in an exponential-linear manner. This implies that a different h' and β may be needed at different frequencies to match propagation results to a model. If we desire to obtain an accurate electron density at all altitudes *D* region altitudes, future work will need to expand beyond the traditional Wait and Spies 2 parameter assumption.

The unique agreement with the model from 5 to 30 kHz, combined with the stability of the processed results and well-validated simulations of LWPC allows us to generally infer ionospheric information sensitive to those frequencies. Importantly, this example utilizes the general waveform shape and does not rely on feature searching, a cornerstone, and limitation, in all current *D* region sferic-based work. For example, early studies from Cummer et al. (1998) and Cheng et al. (2006) utilize a modal amplitude structure for a specific source-receiver geometry. Furthermore, these studies use only amplitude information, without considering phase. The phase minimization space has different shaped contours than amplitude and may be important in observing ionospheric changes more sensitive to phase. In addition, broadband amplitude and phase taken together may be needed to understand the discrepancy between measured and simulated sferic broadband phase during a solar flare. Furthermore, the additional information can reduce error in model-based ionospheric inferences since both measurements are well validated by LWPC results.

The results from Han and Cummer (2010a, 2010b) and Han et al. (2011) are dependent on specific sferic amplitude spectral features and subsequently specific source-receiver geometry which are not generally available for modeling. Lay and Shao (2011b) and later studies (Lay & Shao, 2011a; Lay et al., 2014; Shao et al., 2013) utilize features of the time domain waveform that is applicable to specific distances of source-receiver path, namely, the source occurring far enough away to receive a coherent ionospheric hop, but not too far so that the ionospheric hop arrives at a similar time as the ground wave. By considering general spectral shape including any modal interference in the waveforms we can extend the ionospheric inference to be generally applicable. This ability combined with the full range of time domain and amplitude/phase information for both sferic magnetic field components and the wide space and time distribution of these sources will allow for greater spatial studies and information about the *D* region of the ionosphere compared previous studies.

Although these path-averaged inferences contain coded information over their entire respective source-receiver path, individual results may generally average out local ionospheric changes such as an early/fast, lightning-induced electron precipitation, or solar eclipse. However, with many path-averaged measurements much of the underlying information can be recovered (e.g., Clilverd et al., 2001). In addition, although LWPC utilizes averaged conditions this is only necessary over discrete segments of a path, and therefore local perturbations can in general be accounted for. Furthermore, measurements could be combined with tomographic techniques which are concerned with transforming 1-D path-averaged scans into 2-D images allowing for greater spatial studies of local and large-scale disturbances derived from path-averaged results. This is similar to the central ideas utilized in computed tomography scans, as previously discussed concerning sferic-based remote sensing (Cummer et al., 1998) and already performed for 3-D studies in the *E* and *F* regions of the ionosphere (Yao et al., 2014).

5. Summary

Lightning is a powerful impulsive and broadband source of VLF/LF radiation which is sensitive to the current state of the *D* region ionosphere due to its reflection from this region. These lightning-generated signals or sferics are spread broadly in space and time across the globe, allowing for greater spatial monitoring of the ionosphere when compared to VLF single-frequency transmitters.

Even the best lightning locating networks have small errors in location and time (e.g., 1–4 km for GLD360) of occurrence which create difficulties in recovering an accurate estimate of the time and spectral characteristics of a sferic. The techniques we described recover high-quality sferic information even though nothing is precisely known about the nature of the individual lightning strokes or the error statistics of lightning location networks. We demonstrate the utility of this technique by comparing measured data to cases of known ionospheric stability and variability.

Sferics have been utilized to remotely sense the *D* region by using both amplitude spectra and time-based techniques for a small number of geometries. But the current techniques are dependent on specific geometries and have not utilized the full lightning data set. Future work will focus on producing ionospheric inferences, such as the Wait and Spies parameters (h', β) by comparing to a model such as LWPC as described, and applying the full range of data for spatial studies that have not been possible before. This future work will utilize the full breadth of information recovered by the processing technique outlined in this study, including Bϕ and Br information for time domain sferics and amplitude/phase spectra.

Acknowledgments
This research was supported by the National Science Foundation under grant AGS 1451142 to the Georgia Institute of Technology. We are very grateful to the Pisgah Astronomical Research Institute and to its staff for their continued support and collaboration. We thank Vaisala, Inc for providing GLD360 data under a cooperative agreement. VLF/LF data can be obtained by contacting Morris Cohen, mcohen@gatech.edu. GLD360 data are commercially available and can be obtained by contacting Vaisala, Inc. GOES data are publicly available at https://www.ngdc.noaa.gov/stp/satellite/goes/dataaccess.html.

References

Alfonsi, L., Kavanagh, A. J., Amata, E., Cilliers, P., Correia, E., Freeman, M., et al. (2008). Probing the high latitude ionosphere from ground-based observations: The state of current knowledge and capabilities during IPY (2007–2009). *Journal of Atmospheric and Solar-Terrestrial Physics*, *70*(18), 2293–2308.

Bilitza, D., McKinnell, L.-A., Reinisch, B., & Fuller-Rowell, T. (2011). The International Reference Ionosphere today and in the future. *Journal of Geodesy*, *85*(12), 909–920.

Bruce, C., & Golde, R. (1941). The lightning discharge. *The Journal of The Institution of Electrical Engineers*, *88*(6), 487–505.

Carvalho, F. L., Uman, M. A., Jordan, D. M., Hill, J. D., Cummer, S. A., Kotovsky, D. A., & Moore, R. C. (2017). *Triggered lightning sky waves, return stroke modeling, and ionosphere effective height* (Vol. 122, pp. 3507–3527). https://doi.org/10.1002/2016JD026202

Cheng, Z., Cummer, S. A., Baker, D. N., & Kanekal, S. G. (2006). Nighttime d region electron density profile and variabilities inferred from broadband measurements using vlf radio emissions from lightning. *Journal of Geophysical Research*, *111*, A05302. https://doi.org/10.1029/2005JA011308

Chrissan, D. A., & Fraser-Smith, A. C. (1996). Seasonal variations of globally measured ELF/VLF radio noise. *Radio Science*, *31*(5), 1141–1152.

Christian, H. J., Blakeslee, R. J., Boccippio, D. J., Boeck, W. L., Buechler, D. E., Driscoll, K. T., et al. (2003). Global frequency and distribution of lightning as observed from space by the optical transient detector. *Journal of Geophysical Research*, *108*(D1), 4005. https://doi.org/10.1029/2002JD002347

Clilverd, M. A., Rodger, C. J., Thomson, N. R., Lichtenberger, J., Steinbach, P., Cannon, P., & Angling, M. J. (2001). Total solar eclipse effects on VLF signals: Observations and modeling. *Radio Science*, *36*(4), 773–788. https://doi.org/10.1029/2000RS002395

Cohen, M. B., Inan, U. S., & Paschal, E. W. (2010). Sensitive broadband ELF/VLF radio reception with the awesome instrument. *IEEE Transactions on Geoscience and Remote Sensing*, *48*(1), 3–17.

Cummer, S. A., Inan, U. S., & Bell, T. F. (1998). Ionospheric *D* region remote sensing using VLF radio atmospherics. *Radio Science*, *33*(6), 1781–1792.

Cummins, K. L., & Murphy, M. J. (2009). An overview of lightning locating systems: History, techniques, and data uses, with an in-depth look at the U.S. NLDN. *IEEE Transactions on Electromagnetic Compatibility*, *51*(3), 499–518.

Dahlgren, H., Sundberg, T., Collier, A. B., Koen, E., & Meyer, S. (2011). Solar flares detected by the new narrowband VLF receiver at SANAE IV. *South African Journal of Science*, *107*(9-10), 1–8.

Dennis, A. S., & Pierce, E. T. (1964). The return stroke of the lightning flash to Earth as a source of VLF atmospherics. *Radio Science*, *68D*(7), 777–794.

Dowden, R. L., Brundell, J. B., & Rodger, C. J. (2002). {VLF} lightning location by time of group arrival (TOGA) at multiple sites. *Journal of Atmospheric and Solar-Terrestrial Physics*, *64*(7), 817–830. https://doi.org/10.1016/S1364-6826(02)00085-8

Ferguson, J. A. (1998). Computer programs for assessment of long-wavelength radio communications (Tech. Rep. 3030): Space and Naval Warfare Systems Center, San Diego.

Ferguson, J. A., & Snyder, F. (1980). Approximate Vlf/Lf waveguide mode conversion model. Computer applications: FASTMC and BUMP (Tech. Rep.). Naval Ocean Systems Center, San Diego, CA.

Friedrich, M., & Torkar, K. M. (2001). FIRI: A semiempirical model of the lower ionosphere. *Journal of Geophysical Research*, *106*(A10), 21,409–21,418. https://doi.org/10.1029/2001JA900070

Gross, N. C., Cohen, M. B., Said, R. K., & Golkowski, M. (2018). Polarization of narrowband VLF transmitter signals as an ionospheric diagnostic. *Journal of Geophysical Research: Space Physics*, *123*, 901–917. https://doi.org/10.1002/2017JA024907

Grubor, D. P., Šulić, D. M., & Žigman, V. (2008). Classification of X-ray solar flares regarding their effects on the lower ionosphere electron density profile. *Annales Geophysicae*, *26*, 1731–1740.

Han, F., & Cummer, S. A. (2010a). Midlatitude daytime *D* region ionosphere variations measured from radio atmospherics. *Journal of Geophysical Research*, *115*, A103314. https://doi.org/10.1029/2010JA015715

Han, F., & Cummer, S. A. (2010b). Midlatitude nighttime D region ionosphere variability on hourly and monthly time scales. *Journal of Geophysical Research*, *115*, A09323. https://doi.org/10.1029/2010JA015437

Han, F., Cummer, S. A., Li, J., & Lu, G. (2011). Daytime ionospheric D region sharpness derived from VLF radio atmospherics. *Journal of Geophysical Research*, *116*, A05314. https://doi.org/10.1029/2010JA016299

Helliwell, R. A., Katsufrakis, J. P., & Trimpi, M. L. (1973). Whistler-induced amplitude perturbation in VLF propagation. *Journal of Geophysical Research*, *78*(22), 4679–4688.

Higginson-Rollins, M. A., & Cohen, M. B. (2017). Exploiting LF/MF signals of opportunity for lower ionospheric remote sensing. *Geophysical Research Letters*, *44*, 8665–8671. https://doi.org/10.1002/2017GL074236

Hutchins, M. L., Holzworth, R. H., & Brundell, J. B. (2014). Diurnal variation of the global electric circuit from clustered thunderstorms. *Journal of Geophysical Research: Space Physics*, *119*, 620–629. https://doi.org/10.1002/2013JA019593

Inan, U. S., Bell, T. F., & Rodriguez, J. V. (1991). Heating and ionization of the lower ionosphere by lightning. *Geophysical Research Letters*, *18*(4), 705–708.
Inan, U. S., Cummer, S. A., & Marshall, R. A. (2010). A survey of ELF and VLF research on lightning-ionosphere interactions and causative discharges. *Journal of Geophysical Research*, *115*, A00E36. https://doi.org/10.1029/2009JA014775
Jones, D. (1970). Electromagnetic radiation from multiple return strokes of lightning. *Journal of Atmospheric and Terrestrial Physics*, *32*(6), 1077–1093. https://doi.org/10.1016/0021-9169(70)90119-4
Kintner, P. M., Brittain, R., Kelley, M. C., Carpenter, D. L., & Rycroft, M. J. (1983). In situ measurements of transionospheric VLF wave injection. *Journal of Geophysical Research*, *88*(A9), 7065–7073. https://doi.org/10.1029/JA088iA09p0706
Kockarts, G. (2002). Aeronomy, a 20th century emergent science: The role of solar Lyman series. *Annales Geophysicae*, *20*, 585–598.
Kolarski, A., & Grubor, D. (2014). Sensing the Earth's low ionosphere during solar flares using VLF signals and GOES solar X-ray data. *Advances in Space Research*, *53*, 1595–1602. https://doi.org/10.1016/j.asr.2014.02.022
Lay, E. H., & Shao, X.-M. (2011a). Multi-station probing of thunderstorm-generated *D*-layer fluctuations by using time-domain lightning waveforms. *Geophysical Research Letters*, *38*, L23806. https://doi.org/10.1029/2011GL049790
Lay, E. H., & Shao, X.-M. (2011b). High temporal and spatial-resolution detection of *D*-layer fluctuations by using time-domain lightning waveforms. *Journal of Geophysical Research*, *116*, A01317. https://doi.org/10.1029/2010JA016018
Lay, E. H., Shao, X.-M., & Jacobson, A. R. (2014). D region electron profiles observed with substantial spatial and temporal change near thunderstorms. *Journal of Geophysical Research: Space Physics*, *119*, 4916–4928. https://doi.org/10.1002/2013JA019430
Le Vine, D. M. (1980). Sources of the strongest RF radiation from lightning. *Journal of Geophysical Research*, *85*(C7), 4091–4095. https://doi.org/10.1029/JC085iC07p04091
Lyu, F., Cummer, S. A., & McTague, L. (2015). Insights into high peak current in-cloud lightning events during thunderstorms. *Geophysical Research Letters*, *42*, 6836–6843. https://doi.org/10.1002/2015GL065047
McRae, W. M., & Thomson, N. R. (2000). VLF phase and amplitude: Daytime ionospheric parameters. *Journal of Atmospheric and Solar-Terrestrial Physics*, *62*, 609–618.
McRae, W. M., & Thomson, N. R. (2004). Solar flare induced ionospheric D-region enhancements from VLF phase and amplitude observations. *Journal of Atmospheric and Solar-Terrestrial Physics*, *66*, 77–87. https://doi.org/10.1016/j.jastp.2003.09.009
Megill, L. R., Adams, G. W., Haslett, J. C., & Whipple, E. C. (1971). Measurement of the effective electron loss rates in the *D* region during polar cap absorption events. *Journal of Geophysical Research*, *76*(19), 4587–4595. https://doi.org/10.1029/JA076i019p04587
Mitra, A. P. (1964). *Ionospheric effects of solar flares*. New York: Springer.
Morfitt, D. (1977). Effective electron density distributions describing VLF/LF propagation data (Tech. Rep.). San Diego, CA: Naval Ocean Systems Center.
Rakov, A. V., & Uman, A. M. (2003). *Lightning physics and effects*. Cambridge: Cambridge University Press.
Said, R. K. (2009). Accurate and efficient long-range lightning geo-location using a VLF radio atmospheric waveform bank (PhD thesis).
Said, R. K., Inan, U. S., & Cummins, K. L. (2010). Long-range lightning geolocation using a VLF radio atmospheric waveform bank. *Journal of Geophysical Research*, *115*, D23108. https://doi.org/10.1029/2010JD013863
Said, R. K., Cohen, M. B., & Inan, U. S. (2013). Highly intense lightning over the oceans: Estimated peak currents from global GLD360 observations. *Journal of Geophysical Research: Atmospheres*, *118*, 6905–6915. https://doi.org/10.1002/jgrd.50508
Sechrist, C., Mechtly, E., Shirke, J., & Theon, J. (1969). Coordinated rocket measurements on the D-region winter anomaly. I. Experimental results. *Journal of Atmospheric and Terrestrial Physics*, *31*(1), 145–153. https://doi.org/10.1016/0021-9169(69)90088-9
Sechrist, C. J. (1974). Comparisons of techniques for measurements of D-region electron densities. *Radio Science*, *9*(2), 137–149.
Shao, X.-M., & Jacobson, A. R. (2009). Model simulation of very low-frequency and low-frequency lightning signal propagation over intermediate ranges. *IEEE Transactions on Electromagnetic Compatibility*, *51*(3), 519–525. https://doi.org/10.1109/TEMC.2009.2022171
Shao, X.-M., Lay, E. H., & Jacobson, A. R. (2013). Reduction of electron density in the night-time lower ionosphere in response to a thunderstorm. *Nature Geoscience*, *6*(1), 29–33.
Singh, A. K., Singh, A. K., Singh, R., & Singh, R. P. (2013). Solar flare induced D-region ionospheric perturbations evaluated from VLF measurements. *Astrophysics and Space Science*, *350*, 1–9. https://doi.org/10.1007/s10509-013-1699-4
Šulić, D. M., & Srećković, V. A. (2014). A comparative study of measured amplitude and phase perturbations of VLF and LF radio signals induced by solar flares. *Serbian Astronomical Journal*, *188*, 45–54. https://doi.org/10.2298/SAJ1488045S
Thomson, N. R. (1993). Experimental daytime VLF ionospheric parameters. *Journal of Atmospheric and Terrestrial Physics*, *55*(2), 173–184.
Thomson, N. R. (2010). Daytime tropical *D* region parameters from short path VLF phase and amplitude. *Journal of Geophysical Research*, *115*, A09313. https://doi.org/10.1029/2010JA015355
Thomson, N. R., & Clilverd, M. A. (2001). Solar flare induced ionospheric D-region enhancements from VLF amplitude observations. *Journal of Atmospheric and Solar-Terrestrial Physics*, *63*, 1729–1737.
Thomson, N. R., Clilverd, M. A., & McRae, W. M. (2007). Nighttime ionospheric *D* region parameters from VLF phase and amplitude. *Journal of Geophysical Research*, *112*, A07304. https://doi.org/10.1029/2007JA012271
Thomson, N. R., & McRae, W. M. (2009). Nighttime ionospheric *D* region: Equatorial and nonequatorial. *Journal of Geophysical Research*, *114*, A08305. https://doi.org/10.1029/2008JA014001
Thomson, N. R., Rodger, C. R., & Clilverd, M. A. (2005). Large solar flares and their ionospheric *D* region enhancements. *Journal of Geophysical Research*, *110*, A06306. https://doi.org/10.1029/2005JA011008
Volland, H. (1995). *Handbook of atmospheric electrodynamics*. Boca Raton, FL: CRC Press.
Wait, J. R., & Spies, K. P. (1964). Characteristics of the Earth-ionosphere waveguide for VLF radio waves (Technichal Note 300). National Bureau of Standards.
Yao, Y., Tang, J., Chen, P., Zhang, S., & Chen, J. (2014). An improved iterative algorithm for 3-D ionospheric tomography reconstruction. *IEEE Transactions on Geoscience and Remote Sensing*, *52*(8), 4696–4706.
Zoghzoghy, F. G. (2015). Statistical analysis and modeling of lightning using radio remote sensing (PhD thesis), Stanford University.